RSC Sustainability

ROYAL SOCIETY OF CHEMISTRY

PAPER

View Article Online
View Journal

Cite this: DOI: 10.1039/d6su00070c

A high power, low temperature molten sodium battery

Michael E. Ureña, Amanda S. Peretti, Stephen J. Percival, Philip S. Mantos, Erik D. Spoerke and Leo J. Small *

Low temperature molten sodium batteries promise low-cost, grid-scale energy storage using earth-abundant materials. To be economically viable, they must demonstrate high current (power) at relevant discharge times. Here a low temperature (135 °C) molten sodium battery with a NaI–$AlCl_3$ molten salt catholyte and NaSICON separator is explored, minimizing cell ohmic resistances and avoiding precipitation reactions in the molten salt catholyte. Operating currents were increased by as much as 100× compared to the energy-dense baseline design (197 Wh kg^{-1} and 248 mAh cm^{-2}). Cells were cycled 100 times at 50 mA cm^{-2} (150 mW cm^{-2}), averaging 99.8% coulombic efficiency and 79.7% energy efficiency for 30% of the theoretical capacity. Charging currents up to 250 mA cm^{-2} (1070 mW cm^{-2}) are demonstrated for 10% of the theoretical capacity. Toward extending the accessible capacity in these high current systems, the volume ratio of catholyte molten salt to a graphite felt current collector was varied, altering (1) the local current density in the graphite felt and (2) the discharge time at a fixed current density. Optimizing the catholyte : felt ratio dramatically increased capacity utilization to 60% (102 mAh cm^{-2}) at 50 mA cm^{-2} (150 mW cm^{-2}) charge and 10 mA cm^{-2} discharge. This catholyte : felt ratio of 1.4 significantly decreased the cell impedance, minimizing electrode blocking effects seen previously in NaI–$AlCl_3$ catholytes. Together, these high areal loadings and impressive power outputs demonstrate how low temperature molten sodium batteries can compete with commercialized sodium systems operating at more than twice the temperature.

Received 5th February 2026
Accepted 24th February 2026

DOI: 10.1039/d6su00070c

rsc.li/rscsus

Sustainability spotlight

Grid-scale energy storage is essential for enhancing the reliability of the electrical grid. Molten sodium batteries promise a low-cost solution, featuring a molten sodium anode, Na-ion selective solid-state separator, and partially molten cathode, all made from abundant materials like Na, S, Si, and Al. However, traditional molten sodium batteries operate at around 300 °C, requiring costly materials and engineering. To realize the cost advantages of low-temperature systems, high-current and high-power operation must be achieved. By increasing the current density for a given cycle time, the ratio of the active to the inactive material increases, reducing costs per kWh. This study discusses a molten sodium battery operating at 135 °C with a NaI–$AlCl_3$ catholyte and NaSICON separator, demonstrating high current and power densities.

Introduction

Molten sodium batteries offer the promise of low-cost energy storage for grid-scale applications. These batteries typically consist of a molten sodium anode, Na-ion selective solid-state separator, and cathode that is at least partially molten. Made from earth abundant materials such as Na, S, Si, and Al, electrochemically active materials are low cost and readily available throughout the globe.[1] Typical molten sodium batteries, however, operate at temperatures near 300 °C.[2–4] These high temperatures promote solubility of species, enhance electrochemical reaction kinetics, and increase conductivity in ion-selective separators, enabling efficient cycling with high areal capacities.[4–6] Indeed, the initial report on sodium–sulfur (Na–S) batteries in 1968 by Kummer and Weber boasted an impressive 680 mA cm^{-2} (1.7 W cm^{-2}) for 340 mAh cm^{-2}.[7] Admittedly, this initial report did not evaluate long-term performance. Estimations of other designs suggest performance metrics up to 500 mA cm^{-2} for up to 500 mAh cm^{-2} at maximum powers on the order of 1000 mW cm^{-2}.5 Despite these admirable performance metrics, molten sodium battery systems are often more expensive than benchmark Li-ion systems.[8]

One strategy to reduce the cost of molten sodium batteries is through the reduction of the operating temperature to <200 °C,[9–11] going as low as 100–110 °C,[12–14] thereby significantly decreasing the system level cost of components such as specialized wiring, hermetic seals, thermal insulation, and heat management.[15,16] Lowering the operating temperature, however, introduces a host of challenges, including specific

Sandia National Laboratories, Albuquerque, NM, 87185, USA. E-mail: ljsmall@sandia.gov

challenges to both the anode-separator interface and cathode chemistry.

At 300 °C, molten sodium readily wets solid-state electrolytes such as the sodium super ion conductor (NaSICON) or β″-Al_2O_3.[17] Superior wetting, high Na^+ conductivity, and high interfacial conductance readily enable efficient, high-current Na transport across the molten Na-electrolyte interface, with currents beyond 1000 mA cm^{-2} reported.[18] Upon reducing the temperature to 100–150 °C, such inherent advantages dissipate; poor wetting, lower conductivities, and low interfacial conductance dominate, decreasing cell efficiency and promoting *trans*-electrolyte sodium shorts at extremely high current densities.[19–24] Fortunately, the scientific community has largely solved these problems. High conductivity compositions of NaSICON boast conductivities >50 mS cm^{-1} at 150 °C.[25–27] A multitude of interfacial coatings designed for NaSICON and/or β″-Al_2O_3 have enabled good sodium wetting and high interfacial conductance for temperatures <200 °C.[28] Various groups have employed coatings leveraging films of polymers,[17] Sn,[29–31] Bi,[30] Pb,[32] and carbon,[33,34] or turned to specific sodium alloys.[9,30]

On the cathode chemistry front, new chemistries must be developed specifically for operation <200 °C, as typical cathode chemistries for molten sodium batteries (*e.g.* Na–S and Zeolite Battery Research Africa (ZEBRA)[35]) will be kinetically sluggish and, in some cases, solidify and be rendered electrochemically inaccessible.[24] Several groups have looked at adapting $NiCl_2$ chemistries typical of ZEBRA[35] batteries,[11,36] or analogous $FeCl_2$-based chemistries.[37] Other groups have used aqueous $I/I_3^-/I_2$ chemistries,[14] ionic liquids,[38] oxygen redox,[39] solid Al metal cathodes,[40] and even molten BiSnIn cathode alloys.[41] Our group has developed a series of fully inorganic, redox-active, molten salt electrolytes based on the I^-/I^{3-} redox couple that are liquid at temperatures as low as 50 °C.[13,42–45] Stable performance has been demonstrated over extended periods of time using realistic discharge times (4–24 h) at 110 °C.[13,46] While the 2.5–5 mA cm^{-2} utilized in these long-term, lab-scale cells are competitive with fast-charging Li-ion chemistries, they are significantly below the 100–200 mA cm^{-2} desirable in high temperature molten sodium systems such as NaS or ZEBRA that do not benefit from the higher geometric surface area designs common to batteries like Li-ion (*e.g.*, jelly rolls).[47]

To realize the inherent cost-benefits of low-temperature molten sodium systems, however, particularly compared with existing high temperature molten sodium battery systems and incumbent Li-ion systems, high current and high-power operation must be demonstrated. The motivation for high current density is primarily one of cost. Molten sodium batteries targeted at grid scale energy storage typically require 4–12 h discharge times characteristic of medium to long duration energy storage.[21,48,49] If higher current density can be achieved for this discharge duration, then a larger areal capacity is accessed. In general, a cell with larger areal capacity will have a higher ratio of the active material to the inactive material (separator, housing, seals, *etc.*), decreasing the cost per kWh, as shown by projections in Fig. S1 for the system described in this report. If currents of 100 mA cm^{-2} can be achieved, active materials costs of \$20 kWh^{-1} and assembled battery costs of \$26 kWh^{-1} might be achieved. To obtain the total required power and energy at the system level (*e.g.* 100 kW/1 MWh), cells can be assembled in series or parallel to meet the application requirements. The design of the individual cell, however, largely sets the ratio of the active to the inactive material – which dramatically affects costs. Similar design criteria have successfully been applied to redox flow batteries, where increasing operating currents were shown to decrease the relative cost of inactive materials in the cell stack (*e.g.* membranes), under many operating conditions.[50]

With this generalized cost analysis in mind, we sought to increase the current and power density in a low temperature molten sodium battery and understand the ultimate limitations in high current (high power) performance. The results presented herein describe the performance and optimization of a molten sodium battery operated at the economically favorable, low temperature of 135 °C using a molten sodium anode separated from a NaI–$AlCl_3$ catholyte by a high-conductivity NaSICON solid-state electrolyte. In this battery the cell half reactions during charge are as follows:

$$\text{(Anode)}\ Na^+ + e^- \rightarrow Na \quad (1)$$

$$\text{(Cathode)}\ 3I^- \rightarrow I_3^- + 2e^- \quad (2)$$

In the molten salt catholyte, the I^--species are complexed to $AlCl_3$ as a Lewis acid–base adduct, forming species such as $AlCl_3I^-$ and $AlCl_3I_3^-$.[13,44,46] Moreover, the cathode reaction in (2) consists of two steps, an electrochemical step (3) and a chemical step (4).[13,44]

$$2I^- \rightarrow I_2 + 2e^- \quad (3)$$

$$I_2 + I^- \rightarrow I_3^- \quad (4)$$

Understanding and overcoming the limitations of cell design and catholyte chemistry enables operation of these batteries at high current density and impressive power density approaching those of commercial NaS or ZEBRA systems, yet at less than half the operating temperature.

Experimental

NaSICON ($Na_{3.4}Zr_{2.0}Si_{2.4}P_{0.6}O_{12}$) synthesis was performed using standard solid-state ceramic processing techniques described in detail elsewhere.[25,46] Briefly, $ZrSiO_4$ (Sigma-Aldrich, −325 mesh), $Na_3PO_4 \cdot 12H_2O$ (Sigma-Aldrich, >98%), SiO_2 (Sigma-Aldrich), and Na_2CO_3 (Sigma-Aldrich) powders were ball-milled in ethanol in a 2 : 0.6 : 0.4 : 0.8 molar ratio and subsequently dried by rotary evaporation before further drying under vacuum overnight. The resulting NaSICON precursor powder was calcined at 1000 °C for 12 h in air. The calcined powder was passed through a 150 μm sieve and uniaxially pressed in a 1–1/8 in. die to 8 ksi, followed by isopressing to 30 ksi. The pressed cylinder was sintered on a bed of NaSICON precursor powder, covered with a crucible and heated in air at 5 °C min^{-1} to 1230 °C, including holds at 400 °C for 2 h and 600 °C for 4 h. The sample was then held at 1230 °C for 12 h before cooling to room

temperature at 5 °C min^{-1}. Phase purity was verified *via* XRD. Na-ion conductivity was typically 3.00–3.75 mS cm^{-1} at 25 °C and 65.1 mS cm^{-1} at 135 °C, as measured using Au-blocking electrodes in air.[25]

After sintering, the cylinder was sliced into 1 mm thick discs (25 mm diameter) using a Buehler IsoMet High Speed Pro saw and polished on one side to 1200 grit using SiC paper and water. After drying overnight at 100 °C in air, the polished side of the NaSICON pellet was sputter-coated with a layer of Sn approximately 170 nm thick and used facing the Na metal, as described previously.[29] Shadow masks were used to define the circular area (1.13 cm^2 for cell G-1 and 1.77 cm^2 for all others) of the Sn coating.

Battery assembly

Batteries were assembled in an Ar-filled glovebox with <0.1 ppm of O_2 and H_2O. Two cell designs were used, depicted in Fig. 1 and summarized in Table 1: an un-optimized glass cell geometry (Cell G-1) consisting of custom glass chambers with W rod current collectors[12,46] and planar cells (Cells P1–P5) consisting of a 316 stainless steel anode chamber and a PTFE cathode chamber. In both cases the anode and cathode chambers were separated by a NaSICON separator. NaSICON was sealed to the anode chamber with an EPDM o-ring, while the cathode chamber was sealed to NaSICON with a PTFE o-ring. The anode consisted of Sn-saturated metallic Na (6.7×10^{-3} wt% Sn). Na was saturated in Sn to prevent dissolution of the Sn thin film deposited on the NaSICON.[29] The catholyte chamber contained NaI (ultra-dry, 99.99%, Alfa Aesar), $AlCl_3$ (ultra-dry, 99.99%, Alfa Aesar), and I_2 (ultra-dry, 99.998%, Alfa Aesar). The specific masses of each reagent used in each cell are compiled in Table 1. All cells were assembled at a 7.5% state of charge (SoC), based on a theoretical capacity assuming the reaction $3I^- \rightarrow I_3^- + 2e^-$. The cathode current collector consisted of graphite felt (SIGRACELL, GFD 2.5 and/or 4.6) thermally activated by heating at 500 °C for 15 h in air. A Mo wire (annealed, 99.95%, Alfa Aesar) or Mo mesh (McMaster-Carr, 0.012″ wire 20 × 20 mesh) was used to improve electrical contact to the graphite felt (see Fig. 1). Mo mesh was etched in concentrated NH_4OH at 60 °C for 4 h to reduce surface oxides. In all cases, the cells were loaded with active materials, sealed, inverted, and melted at 135 °C for 12 hours. Afterwards, the glass cells were flipped upright, allowed to equilibrate for 4 hours, and testing was commenced. For the planar cells, after flipping upright, the Mo rod cathode current collector was loosened in its fitting and pressed downwards to apply a slight pressure on the Mo mesh/graphite felt. This resulted in the graphite felt being compressed to approximately 80% of its original thickness for both 2.5 and 4.6 mm felts. In all cases, no intentional pressure was applied to the sodium or sodium-NaSICON interface.

Table 1 Masses of reagents used to assemble each battery in this work. "CC thickness" describes the thickness of the graphite felt current collector (CC). Cell area was 1.13 cm^2 for G-1 and 1.77 cm^2 for all planar cells (P-1–P-5)

Cell ID	Na/g	$AlCl_3$/g	NaI/g	I_2/g	Capacity/mAh	CC thickness/mm
G-1	1.50	1.39	2.23	0.10	280	4.6
P-1	0.88	1.00	1.59	0.07	200	2.5
P-2	0.92	1.50	2.39	0.11	300	2.5
P-3	0.96	1.50	2.39	0.11	300	4.6
P-4	0.90	1.25	1.99	0.09	250	4.6
P-5	0.93	1.00	1.59	0.07	200	4.6

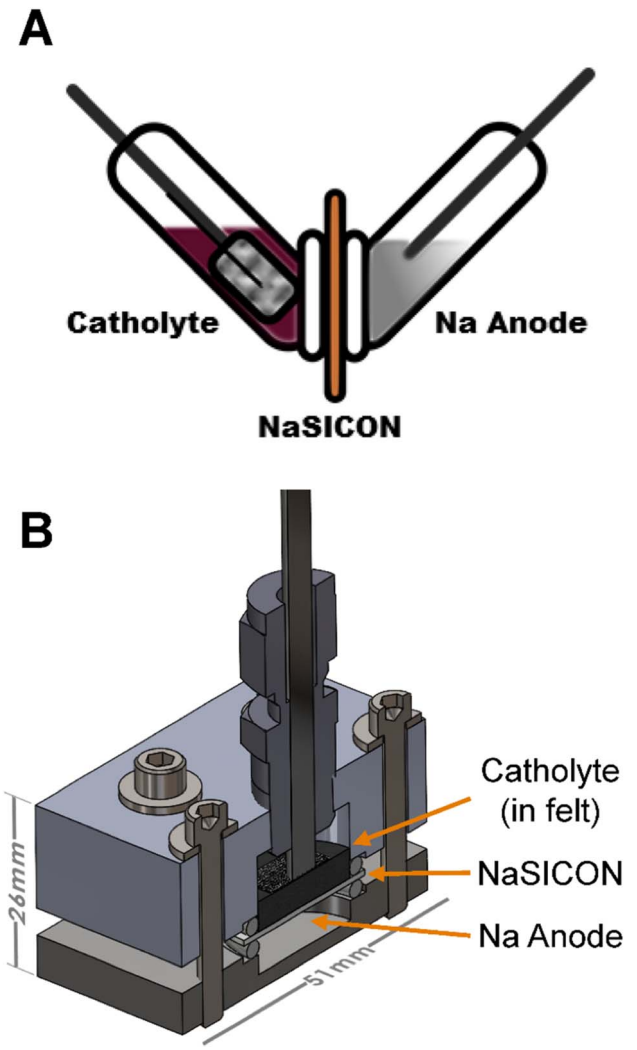

Fig. 1 Schematic of (A) original cell design compared to (B) revised planar cell design. (A) Reproduced with permission from ref. 46.

Battery testing and electrochemical characterization

Electrochemical measurements were made with the batteries inside a convection oven at 135 °C inside an Ar-filled glovebox. The galvanostatic intermittent titration technique (GITT) was performed on an Arbin LBT21084 using 0.25 h pulses of 2.5 mA cm^{-2} followed by 0.25 h rests at the open circuit voltage (OCV). Galvanostatic battery testing was also performed with an Arbin LBT21084 battery tester. Rate testing consisted of galvanostatic cycling for 10% of the theoretical capacity at progressively increasing current densities (1, 2.5, 5, 10, 17.5, 25, 50, and 100

mA cm^{-2}). Capacity utilization testing was conducted by successively increasing the capacity cycled in increments of 10% of the theoretical capacity, starting at the as-assembled 7.5% SoC and halting the test if the voltage limits of 4.2 (charge) or 2.4 V (discharge) were exceeded (*e.g.* Cycle 1 : 7.5–17.5% SoC, Cycle 2 : 7.5–27.5% SoC, Cycle 3 : 7.5–37.5% SoC, *etc.*). Here a 50 mA cm^{-2} charge current and 10 mA cm^{-2} discharge current were used. Electrochemical impedance spectroscopy (EIS) measurements were performed using a Solartron ModuLab XM ECS potentiostat or Gamry Interface 1010E from 1 MHz or 100 kHz to 100 mHz at 10 mV_{rms} AC amplitude and 0 V_{DC} *vs.* OCV. All data have been normalized to the contact area of the Na-NaSICON interface defined by the Sn coating: 1.13 cm^2 for cell G-1 and 1.77 cm^2 for cells P-1–P-5.

Results and discussion

A series of experiments were designed and executed to identify the maximum current density, specific power, and areal capacities achievable using a molten sodium battery at 135 °C employing the I^-/I_3^- redox couple in a NaI–$AlCl_3$ catholyte. First, the maximum accessible capacity was measured using the GITT under low current conditions. The lab-scale cell design was then optimized to minimize the cell resistance, enabling cycling at 50–250 mA cm^{-2} and extended cycling at 50 mA cm^{-2} and 80% energy efficiency for 30% of the theoretical capacity. Limitations to higher current densities were attributed to previously identified mechanisms, whereby precipitated I_2 or NaI may "block" the electrode at high current densities and/or long discharge times.[42,45] To circumvent these limitations, the volume ratio of (molten salt catholyte) : (graphite felt current collector) was varied. This ratio affects (1) the local current density for the I^-/I_3^- redox at the current collector and (2) the time required to access the theoretical capacity at a given current density (*i.e.* the cell capacity). Identification of a critical catholyte : felt ratio of 1.4 enabled charging at 50 mA cm^{-2} while increasing the maximum accessible capacity from 40 to 60% of the theoretical capacity.

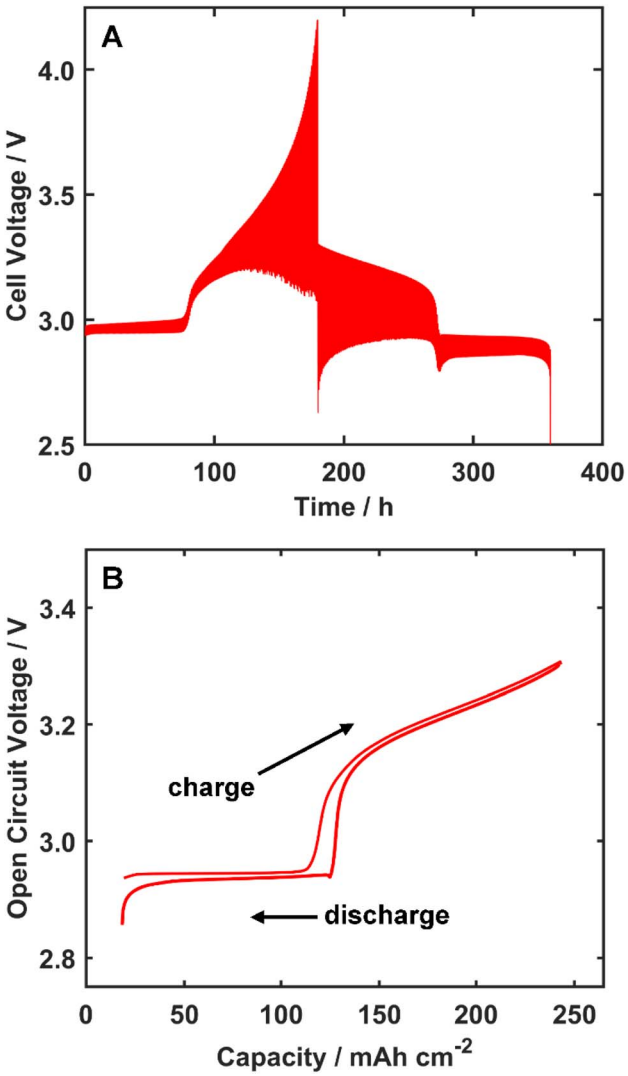

Fig. 2 GITT measurements on a 248 mAh cm^{-2} NaI–$AlCl_3$ battery G-1 at 135 °C. (A) Voltage as a function of time for the entire test. (B) Open circuit voltage recorded at the end of each rest step. Capacity starts at 19 mAh cm^{-2} to account for the as-built state of charge.

Theoretical capacity is achieved at low rates

The capacity obtainable at low current density was measured to set an upper bound for the maximum capacity and energy density obtainable in this energy storage system. GITT measurements were performed at 135 °C, with alternating pulses of 2.5 mA cm^{-2} for 0.25 h, followed by 0.25 h of rest. The results, plotted in Fig. 2, demonstrate that 92.5% of the theoretical capacity can be accessed, equating to a respectable 197 Wh kg^{-1} at a very high areal loading of 0.231 Ah cm^{-2} Considering that the battery was assembled at 7.5% state of charge (SoC), practically all theoretical capacity was accessed. The plot of open circuit *vs.* capacity in Fig. 2B reveals two distinct regions in the battery cycling, consistent with reports on other NaI-Lewis acid systems.[13] Initially, the concentration of I^--containing species in the melt (*e.g.* $AlCl_3I^-$) is buffered by the excess NaI, creating a flat voltage profile for iodide oxidation (eqn (2)).[46] The cell voltage begins to increase as this NaI is consumed, higher order polyiodides are generated and oxidized (*e.g.* $AlCl_3I_3^- \rightarrow AlCl_3I^- + I_2 + e^-$), and the bulk electrolyte composition begins to significantly change. During charge the electrolyte composition loses Na^+ once all solid-phase NaI is consumed. As the cell is discharged, the processes and associated voltage are seen in reverse order, as expected. Nearly 100% of the theoretical capacity can be obtained at both low temperatures (135 °C) and high areal loadings (0.231 Ah cm^{-2}), which is very promising toward maximizing usable capacity at high current and power densities.

Cell redesign minimizes ohmic resistances and enables higher rates

The lab-scale cells used for GITT testing and in other previous work, displayed in Fig. 1A, were designed for ease of assembly and visual verification of interfacial wetting. These cells contain

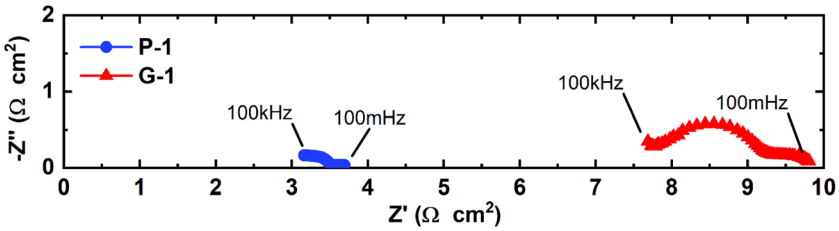

Fig. 3 Comparison of Nyquist plots of the original glass (G-1) and revised planar (P-1) designs, demonstrating significantly decreased resistance for the planar cell. Cell specifics are outlined in Table 1. All data were recorded at 135 °C.

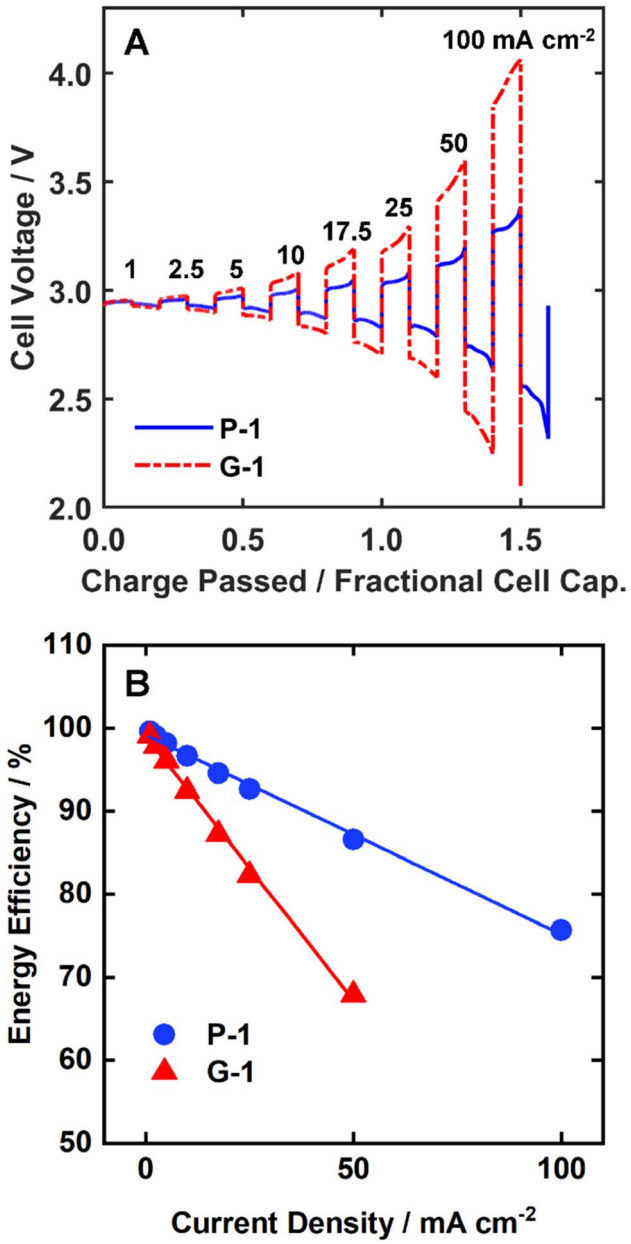

Fig. 4 (A) Rate performance of original glass (G-1) and revised planar (P-1) cell designs under galvanostatic cycling conditions. Each cell was charged and discharged at the listed current density for 10% of the cell's theoretical capacity (20% per cycle) and stopped if the voltage limits of 4.2 or 2.2 were surpassed. (B) Energy efficiency from rate tests. All data were recorded at 135 °C.

a relatively large volume of the catholyte between the catholyte current collector and the NaSICON separator. Accordingly, the ohmic resistance of the cell is relatively large, as seen in the Nyquist plot of cell G-1 in Fig. 3. Nyquist plots from these batteries contain two arcs in the complex impedance plane. The higher frequency arc is related to the Na-NaSICON interface, while the lower frequency arc is characteristic of the NaSICON-catholyte interface.[29,46] The displacement along the Z' axis is related to the ohmic resistance of the cell, including the bulk electrolyte resistance, Na^+ transport through the NaSICON, and electronic transport through the bulk sodium and current collectors. For cell G-1, the ohmic resistance (~7.5 Ω cm^2) represents a large fraction of the total impedance (~10 Ω cm^2), effectively dissipating power through the ohmic cell components, rather than performing useful electrochemical work.

In an effort to reduce this relatively large series impedance, the lab-scale cell was redesigned to a planar configuration, with a schematic shown in Fig. 1B. The resulting impedance data are plotted in Fig. 3 as cell P-1. This design has two major advantages: (1) the graphite felt current collector is directly against the NaSICON separator, minimizing the volume of the catholyte between the NaSICON and current collector and (2) a Mo rod can be used to apply compression to the graphite felt *via* Mo mesh directly over the felt. Advantage (1) resulted in the ohmic resistance of the cell decreasing from 7.5 Ω cm^2 to less than 3 Ω cm^2, while (2) significantly reduced the NaSICON-catholyte interfacial impedance (width of the low frequency arc), improving contact and charge transport across the interface. Compressing graphite felt is widely known to increase its electronic conductivity, at the expense of decreased effective permeability.[51] The impedance of the Na-NaSICON interface (high frequency arc) also decreased which is attributed to more complete wetting of both liquids (Na and the catholyte) on both sides of the NaSICON, though variability of the interfacial Sn-coating on the Na-side could also have a minor effect.

Cells P-1 and G-1 were subjected to galvanostatic cycling at increasing rates from 1–100 mA cm^{-2} for 10% of their theoretical capacities. The results are plotted in Fig. 4A. Cell P-1 successfully completed 100 mA cm^{-2}, while cell G-1 could only complete 50 mA cm^{-2} without exceeding the voltage limits. The resulting energy efficiency from each current level is plotted in Fig. 4B. Here the revised cell P-1 clearly has an advantage, enabling high current (100 mA cm^{-2}) operation at 75.7% energy efficiency. Because the rate tests occurred at 100% coulombic efficiency, all changes in energy efficiency may be attributed to

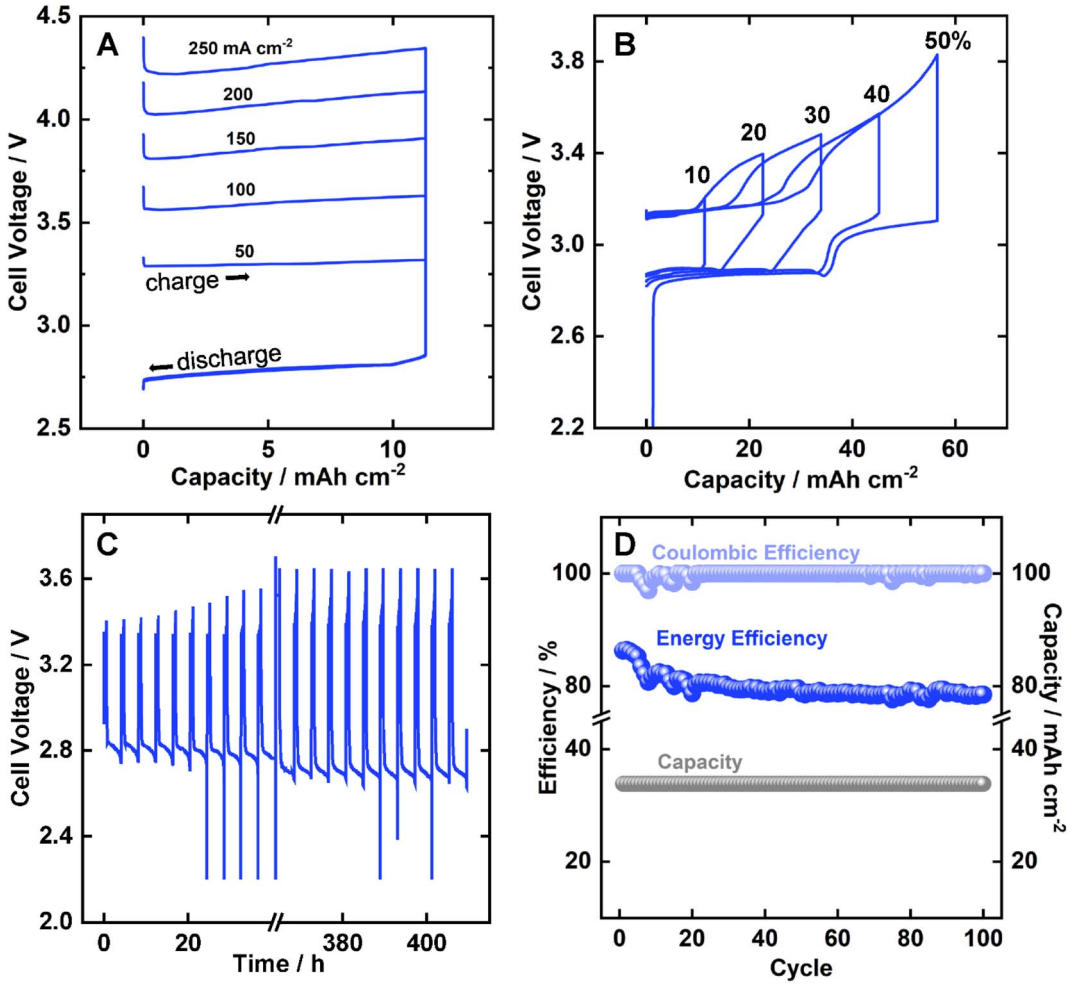

Fig. 5 Performance of planar cell P-1. (A) Voltage profiles under high current galvanostatic cycling at 10% capacity utilization (7.5 ↔ 17.5% SoC) and constant 10 mA cm^{-2} discharge. (B) Voltage profile at increasing depths of discharge at 50 mA cm^{-2} charge and 10 mA cm^{-2} discharge. (C) Long term testing at 50 mA cm^{-2} charge, 10 mA cm^{-2} discharge and 30% capacity utilization (33.9 mAh cm^{-2}). (D) Coulombic and energy efficiencies from (C). All tests were conducted at 135 °C.

voltage efficiency. Thus, the decreased cell impedance observed in EIS translates well into increased energy efficiency for practical battery operation.

Planar cell performance benchmarking

Having minimized the cell resistance to enable efficient, high-current operation at relatively low depth of discharge, a series of experiments were performed to understand the highest achievable current density and capacity. Rate capability was assessed by cycling 10% of the theoretical capacity at increasing current densities. In the rate tests in Fig. 4, all cells failed on discharge, consistent with fundamental 3-electrode studies which identified discharge as more challenging than charge due to NaI precipitation.[45] Fixing the discharge current to 10 mA cm^{-2}, charging currents up to 250 mA cm^{-2} (1070 mW cm^{-2}) were demonstrated on Cell P-1, plotted in Fig. 5A and S2. Such high currents and powers highlight the fast-charging ability of the NaI–$AlCl_3$ catholyte, competitive with higher temperature molten sodium systems. The asymmetry in charge *vs.* discharge is well-suited for grid-scale utility, where rapid charging maximizes the availability of the stored electricity which can be discharged as needed over longer time periods.

Achievable capacity at an aggressive 50 mA cm^{-2} charge and 10 mA cm^{-2} discharge was evaluated by sequentially cycling the cell to increasingly higher states of charge (SoC), starting with the as-assembled 7.5% SoC. These data, plotted in Fig. 5B, indicate that the cell may be easily charged an additional 50% of its theoretical capacity (200 mAh) without hitting the 4.2 V limit, but on discharge the equivalent 100 mAh charged cannot be extracted. Thus, only 40% of the theoretical capacity (80 mAh) can be fully cycled under these conditions. Similar to the rate tests, NaI precipitation and electrode blocking are implicated as the reasons for limited discharge.[45] After holding at OCV for >0.25 h to enable solubilization of NaI, the remaining capacity can be discharged. This result shows that the impediment is not irreversible degradation, but rather a kinetic limitation of this chemistry in this configuration. Nevertheless, 40% of the theoretical capacity equates to 45 mAh cm^{-2}, competitive with reports throughout the literature and a good starting point for further improvement.

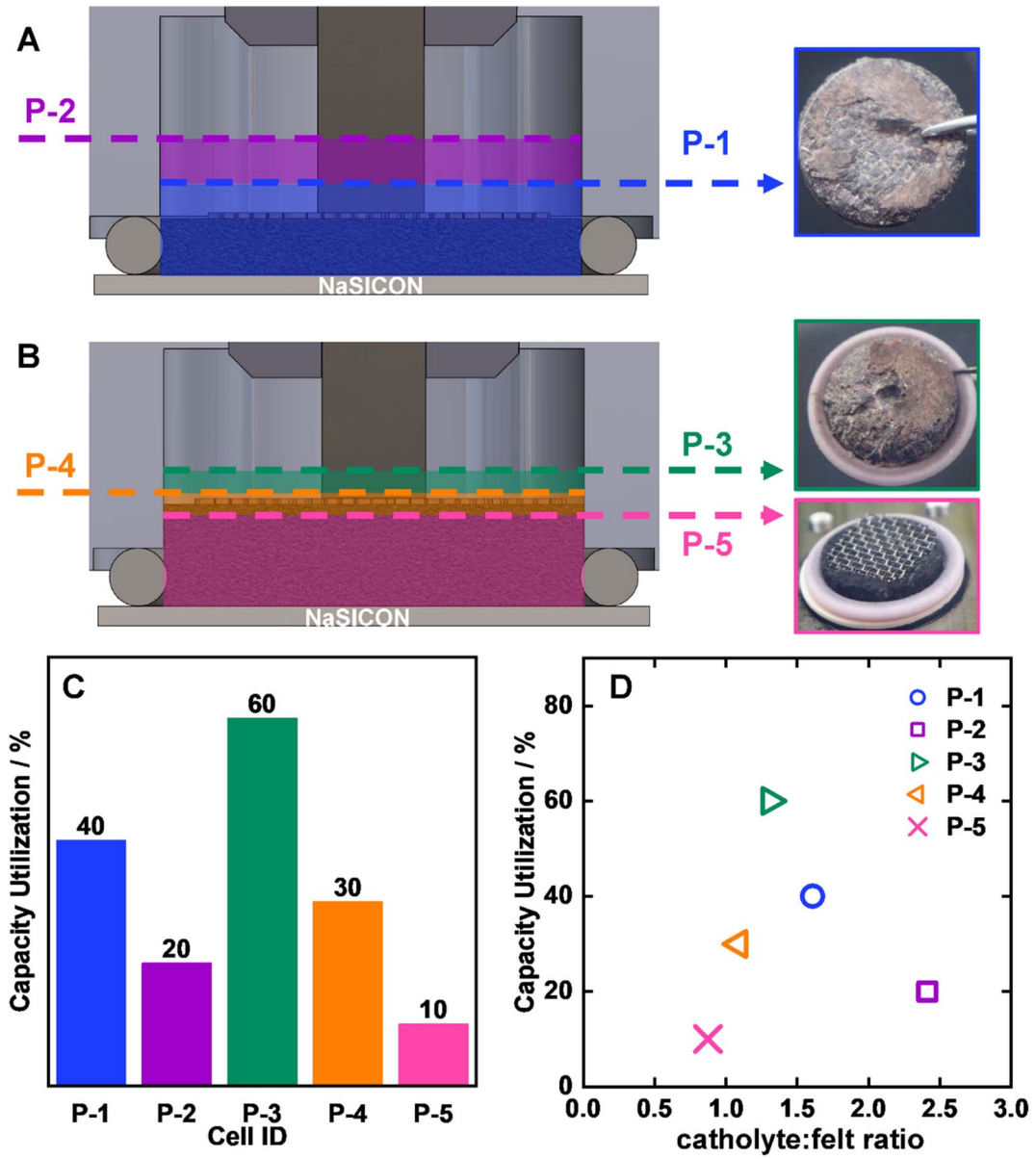

Fig. 6 Optimization of the volume ratio of catholyte molten salt to graphite felt ("catholyte : felt ratio"). Schematics and select photographs depicting the volume of molten salt compared to graphite felt (A) 2.5 mm and (B) 4.6 mm thick. (C) Maximum percentage of theoretical capacity accessed during capacity utilization tests, starting at 7.5% state of charge. (D) Capacity utilization compared to the catholyte : felt ratio. All tests were conducted at 135 °C.

Extended cycling performance was evaluated by cycling 100 times under high current charging (50 mA cm^{-2}) and moderate capacity utilization (30%). The results, plotted in Fig. 5C and D, demonstrate stable cycling performance after an initial break-in period, averaging 99.8% coulombic efficiency and 79.7% energy efficiency. No capacity fade was observed under these conditions; 33.9 mAh cm^{-2} was charged and discharged for 100 cycles, though there were occasional times when the battery could not fully complete the final 1–3% of the discharge cycle without exceeding the lower voltage limit of 2.2 V. These instances are reflected in the data points in Fig. 5D where the coulombic efficiency is not 100%, and most of them occur within the first 20 cycles. This behavior is attributed to initial electrode conditioning and "breaking in" of the molten salt electrolyte. Due to the cell assembly process, most of the solid NaI is initially at the side of the graphite felt opposite to that of the NaSICON. During the initial cycling process, the excess NaI is expected to equilibrate throughout the graphite felt as it is dissolved and redeposited.

Optimization of the catholyte to felt ratio

While the cell design P-1 was limited to about 40% capacity utilization at high current, even higher capacity utilization at high current is desired to decrease overall system cost ($ kWh^{-1}). In an effort to minimize the effects of electrode passivation at high current, the relative amounts of the

catholyte and graphite felt (current collector) were varied across five different cell designs. It was hypothesized that decreasing the catholyte : felt ratio by adding more felt should increase the electrochemically active surface area and decrease local current densities, minimizing the possibility of electrode passivation. If too much felt is added, however, there will be insufficient catholyte to wet it. A CAD model was developed for the cell (Fig. 1B) and the salt volume was calculated based on the known mass and density. The resulting height of molten salt was then determined and is diagrammed in Fig. 6A and B for two different felt thicknesses, assuming the manufacturer's stated open porosity of 94 vol%. Cell P-2 (purple squares) has, relatively, the most catholyte, while cell P-5 (pink X's) has the most graphite felt, relatively. The catholyte : felt ratio was visually verified after testing; volume ratios in photographs (Fig. 6A and B) of graphite felt "pucks" removed from batteries are consistent with the predicted relative amounts of the catholyte and graphite felt. The graphite felt "puck" from P-1 displays a thick layer of salt at the top, while that from Cell P-5 is bare; no molten salt reached the top.

All five of these cells (P-1–P-5) were put through the same testing routine of EIS, rate testing, and capacity utilization testing. The results from capacity utilization testing are provided in Fig. 6C and D. As the catholyte : felt ratio increased, the accessible capacity increased from 10% (cell P-5) to 60% (cell P-3). Adding relatively more salt beyond this point resulted in decreased accessible capacity (cells P-1 and P-2). This effect can be rationalized in terms of the time required to discharge this increased capacity with the same surface area of graphite felt, leading to NaI precipitation and electrode blocking on discharge. When the molten salt catholyte is fully discharged it is saturated with excess NaI.[45] Upon discharging the battery from relatively high states of charge, the increased concentration of reduced iodide species near the electrode may precipitate out of the liquid phase. Impedance measurements before and after capacity testing are consistent with this hypothesis, displaying overall increased cell impedance (Fig. S3). It should be noted that this effect is transient, and <0.25 h is typically required for sufficient NaI dissolution to resolve the electrode blocking.[45]

Nevertheless, optimizing the catholyte : felt volume ratio to 1.4× represents the maximum capacity utilization at high current, effectively increasing the maximum capacity utilization from 40% (cell P-1) to 60% (cell P-3).

To better understand how the catholyte : felt ratio influences the cell impedance, the EIS was recorded for all cells before testing. The results are plotted in Fig. 7. Immediately it was seen in Fig. 7A that the cells with the lowest catholyte : felt ratios, cells P-4 and P-5, exhibited the largest cell impedances across all components – ohmic resistance (Z' offset/initial intercept), Na-NaSICON interface (high frequency arc), and NaSICON-catholyte interface (low frequency arc). This high impedance can be attributed to poor contact area between the molten salt and both the NaSICON and graphite felt current collector. Upon increasing the catholyte : felt ratio to the critical ratio of cell P-3, the impedance drastically decreased across all impedance features, as seen in the Nyquist plot in Fig. 7B. Furthermore, increasing the catholyte : felt ratio from cell P-3 to cell P-1 to P-2 resulted in subtle changes in cell impedance. The differences between impedance features in these cells are relatively small (0.5–1 Ω, or 10–20%) and likely represent experimental variability between cell assembly, NaSICON conductivity, and Sn-coating at the Na-NaSICON interface. For example, both P-2 and P-3 share the same high frequency intercept, as their NaSICON separators were cut from the same mother NaSICON cylinder, recorded as having a Na^+ conductivity of 3.02 mS cm^{-1} (25 °C). Cell P-1's separator was cut from a different NaSICON cylinder, recorded at 2.45 mS cm^{-1} (25 °C), increasing the sodium battery's series resistance relative to P-2 and P-3.

All cells also displayed a nearly flat low frequency tail in the Nyquist plots in Fig. 7. This feature is attributed to transport of reactants in the catholyte through the porous graphite felt. Such behavior is consistent with our previous report, where the graphite felt impedance response was isolated in a 3-electrode cell.[46]

The results from rate testing are provided in Fig. S4. The results are consistent with those of capacity testing and EIS in Fig. 6 and 7. Cells P-1, P-2, and P-3 all displayed low overpotentials. P-1 and P-3 were able to cycle 10% of their theoretical capacity at 100 mA cm^{-2} for both charge and discharge, while P-2 could only cycle at 50 mA cm^{-2} before hitting the voltage limit. This limitation is somewhat expected, as cell P-2 has nearly half the graphite felt volume (and electrode surface area) of P-3 and 50% more salt (capacity) than P-1. At a given current density, this means that cell P-2 will operate at twice the local graphite felt current density of P-3 and for 50% longer time than P-1.

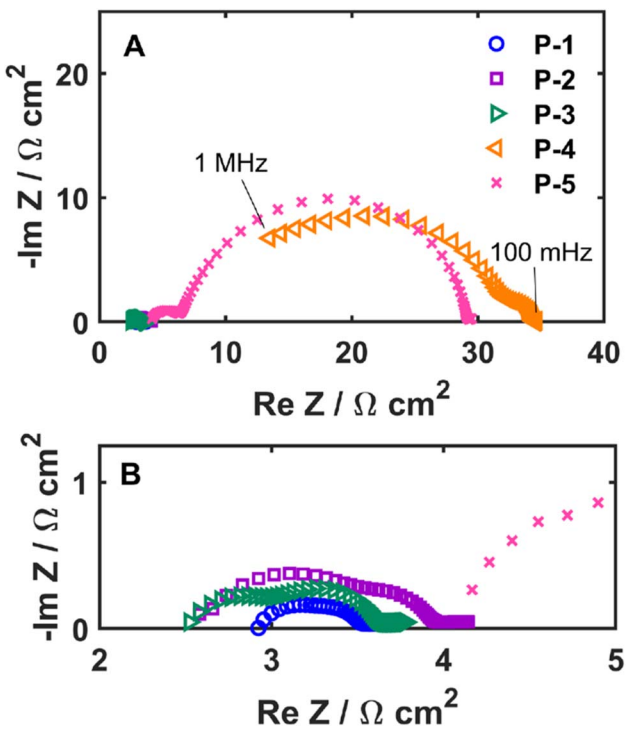

Fig. 7 Nyquist plots for planar batteries with different catholyte : felt ratios, as compiled in Table 1. All tests were conducted at 135 °C. (B) is a zoomed in view of (A).

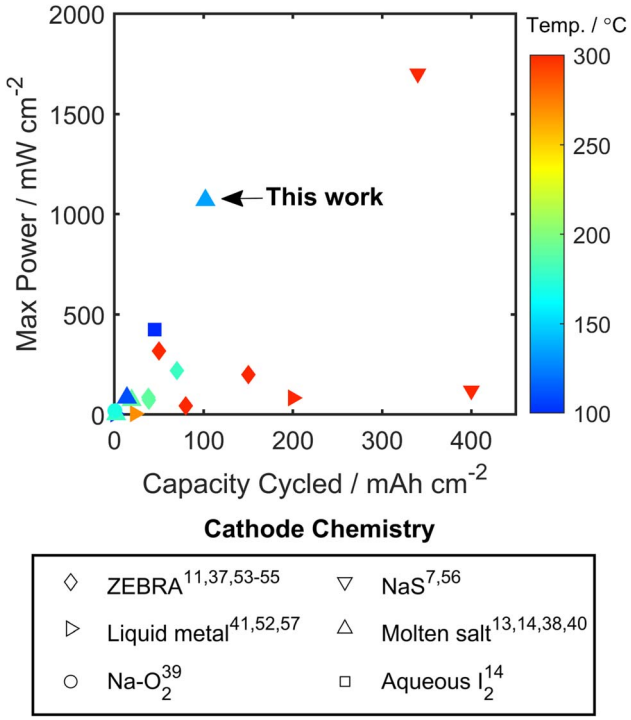

Fig. 8 Comparison of maximum demonstrated power and typical capacity cycled for different molten sodium batteries throughout the literature.[7,11,13,14,37–41,52–57] All batteries operated at ≥300 °C are coded with the same color. The full dataset is compiled in Table S1.

This will create more challenging electrochemical conditions, making it relatively harder to prevent NaI precipitation on discharge. Cells P-4 and P-5 both displayed large overpotentials and could only be cycled to 25 and 50 mA cm^{-2}, respectively. Notably, both cells displayed a "step" in the voltage profile, consistent with the GITT data in Fig. 1. Such behavior would not be expected until higher states of charge and suggests that there was insufficient bulk salt in the graphite felt.

The ability to cycle at 50–100 mA cm^{-2} represents a significant advance in performance for low temperature molten sodium batteries. While this report focused on the cathode design and performance, overall battery performance is controlled by all its interfaces: (1) molten sodium – NaSICON, (2) NaSICON – catholyte, and (3) catholyte – felt. The molten sodium-NaSICON interface was stabilized by use of a previously reported Sn coating.[29] Without this coating, performance at 110–135 °C would be abysmal and NaSICON would be susceptible to sodium metal shorting through the NaSICON electrolyte.[19,20] The NaSICON-catholyte interface was controlled *via* optimization of the Lewis acidity of the catholyte, as described elsewhere.[46] If the catholyte becomes too Lewis acidic, NaSICON surface sites become blocked by emergent salt complexes and charge transfer across this interface is impaired.[46] As such, the molten salt contains excess Lewis base (NaI) to prevent this condition. Most importantly, this work optimizes the battery configuration, minimizing the overall cell resistance and optimizing the relative amounts of the current collector and energy storing catholyte. The combination of high current, high power, and high areal capacity compares favorably to reports on molten sodium batteries across the literature, as seen in Fig. 8 and Table S1. Together, these performance characteristics approach those of commercial high-temperature (~300 °C) sodium batteries.

Conclusion

A high power, low temperature molten sodium battery based on a NaI–$AlCl_3$ catholyte and NaSICON solid-state separator was presented. By optimizing the cell design to reduce the ohmic resistances, high energy efficiency (80%) cycling at high current (50 mA cm^{-2}) was demonstrated and charging pulses as high as 250 mA cm^{-2} (1070 mW cm^{-2}) could be realized. While 92.5% of the theoretical capacity was accessible at low rates (2.5 mA cm^{-2}) in an unoptimized design, 40% of the theoretical capacity was achieved in cell redesign P-1 at 50 mA cm^{-2} charge and 10 mA cm^{-2} discharge. The limited accessible capacity was determined to be due to previously observed electrode blocking by precipitated NaI on discharge. By varying the catholyte : felt ratio, the effective local current density and discharge time could be dramatically improved, enabling up to 60% (102 mAh cm^{-2}) of the theoretical capacity to be achieved at 50 mA cm^{-2} charge and 10 mA cm^{-2} discharge. Such asymmetry is well-suited for grid-related storage, where rapid charging capability improves the accessibility and value of stored energy that can be discharged as needed for improved grid functionality and stability. Regardless, fundamental research is ongoing to identify electrolyte modifications which enable increased discharge currents to further improve the value and utility of this emerging storage technology. Future studies will target understanding the practical scalability of the catholyte : felt ratio for large format (*e.g.* >10 Ah) cells for grid scale energy storage.

Author contributions

This manuscript was written through contributions of all authors. All authors have given approval to the final version of the manuscript.

Conflicts of interest

There are no conflicts to declare.

Data availability

The data supporting this article have been included as part of the supplementary information (SI). Supplementary information: a table comparing performance metrics of molten sodium batteries from the literature and detailed rate test data from all presented cells. See DOI: https://doi.org/10.1039/d6su00070c.

Acknowledgements

The authors thank A. Maraschky for recording GITT data. This material is based upon work supported by the U.S. Department of Energy, Office of Electricity (OE), Energy Storage Division.

Sandia National Laboratories is a multi-mission laboratory managed and operated by National Technology and Engineering Solutions of Sandia, LLC, a wholly owned subsidiary of Honeywell International, Inc., for the U.S. Department of Energy's National Nuclear Security Administration under contract DE-NA0003525. This written work was authored by an employee of NTESS. The employee, not NTESS, owns the right, title, and interest in and to the written work and is responsible for its contents. Any subjective views or opinions that might be expressed in the paper do not necessarily represent the views of the U.S. Department of Energy or the United States Government. The publisher acknowledges that the US Government retains a non-exclusive, paid-up, irrevocable, world-wide license to publish or reproduce the published form of this written work or allow others to do so, for US Government purposes. The DOE will provide public access to results of federally sponsored research in accordance with the DOE Public Access Plan.

References

1 R. C. Hill, M. S. Gross, S. J. Percival, A. S. Peretti, L. J. Small, E. D. Spoerke and Y.-T. Cheng, *Front. Batt. Electrochem.*, 2024, **3**, 1369305.
2 K. B. Hueso, M. Armand and T. Rojo, *Energy Environ. Sci.*, 2013, **6**, 733–749.
3 Z. Wen, Y. Hu, X. Wu, J. Han and Z. Gu, *Adv. Funct. Mater.*, 2013, **23**, 1005–1018.
4 G. Nikiforidis, M. C. M. van de Sanden and M. N. Tsampas, *RSC Adv.*, 2019, **9**, 5649–5673.
5 J. Sudworth and A. R. Tiley, *Sodium Sulphur Battery*, Springer, 1985.
6 P. T. Moseley and D. A. J. Rand, in *Electrochemical Energy Storage for Renewable Sources and Grid Balancing*, ed. P. T. Moseley, Elsevier, 2015, pp. 253–268.
7 J. T. Kummer and N. Weber, *SAE Trans.*, 1968, **76**, 670126–670456.
8 K. Mongird, V. Fotedar, V. Viswanathan, V. Koritarov, P. Balducci, B. Hadjerioua and J. Alam, *Energy Storage Technology and Cost Characterization Report*, Pacific Northwest National Laboratory, 2019.
9 X. Lu, G. Li, J. Y. Kim, D. Mei, J. P. Lemmon, V. L. Sprenkle and J. Liu, *Nat. Commun.*, 2014, **5**, 4578.
10 D. Jin, S. Choi, W. Jang, A. Soon, J. Kim, H. Moon, W. Lee, Y. Lee, S. Son, Y.-C. Park, H. Chang, G. Li, K. Jung and W. Shim, *ACS Appl. Mater. Inter.*, 2019, **11**, 2917–2924.
11 J. Kim, S. H. Jo, S. Bhavaraju, A. Eccleston and S. O. Kang, *J. Electroanal. Chem.*, 2015, **759**, 201–206.
12 M. M. Gross, S. J. Percival, L. J. Small, J. Lamb, A. S. Peretti and E. D. Spoerke, *ACS Appl. Energy Mater.*, 2021, **3**, 11456–11462.
13 M. M. Gross, S. J. Percival, R. Y. Lee, A. S. Peretti, E. D. Spoerke and L. J. Small, *Cell Rep. Phys. Sci.*, 2021, **2**, 10489.
14 M. Holzapfel, D. Wilde, C. Hupbauer, K. Ahlbrecht and T. Berger, *Electrochim. Acta*, 2017, **237**, 12–21.
15 B. L. Spatocco, *Doctor of Philosophy*, Massacusetts Institute of Technology, 2015.
16 H. J. Chang, X. Lu, J. F. Bonnett, N. L. Canfield, S. Son, Y.-C. Park, K. Jung, V. L. Sprenkle and G. Li, *J. Power Sources*, 2017, **348**, 150–157.
17 W. Zhou, Y. Li, S. Xin and J. B. Goodenough, *ACS Cent. Sci.*, 2017, **3**, 52–57.
18 D. Landmann, G. Graeber, M. V. F. Heinz, S. Haussener and C. Battaglia, *Mater. Today Energy*, 2020, **18**, 100515.
19 R. Hill, A. Peretti, L. J. Small, E. D. Spoerke and Y.-T. Cheng, *ACS Appl. Energy Mater.*, 2023, **6**, 2515–2523.
20 R. C. Hill, A. S. Peretti, A. M. Maraschky, L. J. Small, E. D. Spoerke and Y.-T. Cheng, *ACS Appl. Energy Mater.*, 2024, **7**, 810–819.
21 R. C. Hill, A. S. Peretti, L. J. Small, E. D. Spoerke and Y.-T. Cheng, *J. Electrochem. Soc.*, 2024, **171**, 040530.
22 M. J. Counihan, K. S. Chavan, P. Barai, D. J. Powers, Y. Zhang, V. Srinivasan and S. Tepavcevic, *Cell Rep. Phys. Sci.*, 2024, **8**, 64–90.
23 B. Lee, E. Paek, D. Mitlin and S. W. Lee, *Chem. Rev.*, 2019, **119**, 5416–5460.
24 J. Kattelman, J. Moon and D. Chidambaram, *J. Electrochem. Soc.*, 2025, **172**, 020528.
25 A. S. Peretti, E. D. Spoerke, M. E. Ureña, I. D. Dyer, P. A. Salinas, M. A. Rodriguez, P. S. Mantos, J. N. Williard and L. J. Small, *J. Am. Ceram. Soc.*, 2025, e70195, DOI: 10.1111/jace.70195.
26 Q. Ma and F. Tietz, *ChemElectroChem*, 2020, **7**, 2693–2713.
27 K.-T. Tseng, Z. Fang, B. Wang, T. P. Vaida, A. Reach, D. Kwabic, M. Chi, J. B. Wolfenstine and J. Sakamoto, *J. Mater. Chem. A*, 2025, **13**, 34706–34720.
28 C. Yuan, R. Li, X. Zhan, V. L. Sprenkle and G. Li, *Materials*, 2022, **15**, 4636.
29 M. M. Gross, L. J. Small, A. S. Peretti, S. J. Percival, M. A. Rodriguez and E. D. Spoerke, *J. Mater. Chem. A*, 2020, **8**, 17012–17018.
30 K. Ahlbrecht, C. Bucharsky, M. Holzapfel, J. Tübke and M. J. Hoffmann, *Ionics*, 2017, **23**, 1319–1327.
31 D. Reed, G. Coffey, E. Mast, N. Canfield, J. Mansurov, X. Lu and V. Sprenkle, *J. Power Sources*, 2013, **227**, 94–100.
32 H.-J. Chang, X. Lu, J. F. Bonnett, N. L. Canfield, K. Han, M. H. Engelhard, K. Jung, V. L. Sprenkle and G. Li, *J. Mater. Chem. A*, 2018, **6**, 19703–19711.
33 J. M. Weller, H. H. Han, E. Polikarpov, K. Han, V. Shutthanandan, Y. Wang, M. H. Engelhard, K. Jung, D. M. Reed, V. L. Sprenkle and G. Li, *Nano Energy*, 2024, **128**, 109815.
34 M. M. Li, S. Tripathi, E. Polikarpov, N. L. Canfield, K. S. Han, J. M. Weller, E. C. Buck, M. H. Engelhard, D. M. Reed, V. L. Sprenkle and G. Li, *ACS Appl. Mater. Inter.*, 2022, **14**, 25534–25544.
35 J. Coetzer, *J. Power Sources*, 1986, **18**, 377–380.
36 X. Zhan, J. P. Sepulveda, X. Lu, J. F. Bonnett, N. L. Canfield, T. Lemmon, K. Jung, D. M. Reed, V. L. Sprenkle and G. Li, *Energy Storage Mater.*, 2020, **24**, 177–187.
37 X. Zhan, M. E. Bowden, X. Lu, J. F. Bonnett, T. Lemmon, D. M. Reed, V. L. Sprenkle and G. Li, *Adv. Energy Mater.*, 2020, **10**, 1903472.

38 L. Xue, T. G. Tucker and C. A. Angell, *Adv. Energy Mater.*, 2015, **5**, 1500271.
39 Y. G. Zhu, G. Leverick, A. Accogli, K. Gordiz, Y. Zhang and Y. Shao-Horn, *Energy Environ. Sci.*, 2022, **15**, 4636–4646.
40 X. Zhan, J. F. Bonnett, M. H. Engelhard, D. M. Reed, V. L. Sprenkle and G. Li, *Adv. Energy Mater.*, 2020, **10**, 2001378.
41 Y. Ding, X. Guo, Y. Qian and G. Yu, *ACS Cent. Sci.*, 2020, **6**, 2287–2293.
42 S. J. Percival, L. J. Small and E. D. Spoerke, *J. Electrochem. Soc.*, 2018, **165**, A3531–A3536.
43 S. J. Percival, R. Y. Lee, M. M. Gross, A. S. Peretti, L. J. Small and E. D. Spoerke, *J. Electrochem. Soc.*, 2021, **168**, 036510.
44 R. Y. Lee, S. J. Percival and L. J. Small, *J. Electrochem. Soc.*, 2021, **168**, 126511.
45 A. M. Maraschky, S. J. Percival, R. Y. Lee, M. L. Meyerson, A. S. Peretti, E. D. Spoerke and L. J. Small, *J. Electrochem. Soc.*, 2023, **170**, 066504.
46 A. M. Maraschky, M. L. Meyerson, S. J. Percival, D. R. Lowry, S. Meserole, J. N. Williard, A. S. Peretti, M. Gross, L. J. Small and E. D. Spoerke, *J. Phys. Chem. C*, 2023, **127**, 1293–1302.
47 S. Baazouzi, N. Feistel, J. Wanner, I. Landwehr, A. Fill and K. P. Birke, *Batteries*, 2023, **9**, 309.
48 B. Dunn, H. Kamath and J.-M. Tarascon, *Science*, 2011, **334**, 928–935.
49 J. Twitchell, K. DeSomber and D. Bhatnagar, *J. Energy Storage*, 2023, **60**, 105787.
50 V. Viswanathan, A. Crawford, D. Stephenson, S. Kim, W. Wang, B. Li, G. Coffey, E. Thomsen, G. Graff, P. Balducci, M. Kintner-Meyer and V. Sprenkle, *J. Power Sources*, 2014, **247**, 1040–1051.
51 L. D. Brown, T. P. Neville, R. Jervis, T. J. Mason, P. R. Shearing and D. J. L. Brett, *J. Energy Storage*, 2016, **8**, 91–98.
52 W. Ding, Q. Gong, S. Liang, R. Hoffmann, H. Zhou, H. Li, K. Wang, T. Zhang, A. Weisenburger, G. Müller and A. Bonk, *J. Power Sources*, 2023, **553**, 232254.
53 G. Graeber, D. Landmann, E. Svaluto-Ferro, F. Vagliani, D. Basso, A. Turconi, M. V. F. Heinz and C. Battaglia, *Adv. Energy Mater.*, 2021, **31**, 2106367.
54 T. Lan, G. Graeber, L. Sieuw, E. Svaluto-Ferro, F. Vagliani, D. Basso, A. Turconi, C. Battaglia and M. V. F. Heinz, *Adv. Energy Mater.*, 2023, **33**, 2302040.
55 T. Lan, E. Svaluto-Ferro, N. Kovalska, G. Graeber, F. Vagliani, D. Basso, A. Turconi, M. Makowska, G. Blugan, C. Battaglia and M. V. F. Heinz, *Batteries Supercaps*, 2024, **8**, e202400447.
56 M. Kamibayashi and K. Furuta, High Charge And Discharge Cycle Durability of The Sodium Sulfur (NAS) Battery, *Electrical Energy Storage Applications & Technologies*, San Francisco, CA, 2002.
57 B. L. Spatocco, T. Ouchi, G. Lambotte, P. J. Burke and D. R. Sadoway, *J. Electrochem. Soc.*, 2015, **162**, A2729–A2736.